PAPER

Check for updates

Photo-enhanced gas sensing of SnS$_2$ with nanoscale defects†

Wen-Jie Yan,[a] Deng-Yun Chen,[a] Huei-Ru Fuh,*[bc] Ying-Lan Li,[a] Duan Zhang,[a] Huajun Liu,[d] Gang Wu,[a] Lei Zhang, [e] Xiangkui Ren, [e] Jiung Cho,[f] Miri Choi,[g] Byong Sun Chun,[h] Cormac Ó. Coileáin,[a] Hong-Jun Xu,[a] Zhi Wang,[a] Zhaotan Jiang,[a] Ching-Ray Chang*[b] and Han-Chun Wu [*a]

Recently a SnS$_2$ based NO$_2$ gas sensor with a 30 ppb detection limit was demonstrated but this required high operation temperatures. Concurrently, SnS$_2$ grown by chemical vapor deposition is known to naturally contain nanoscale defects, which could be exploited. Here, we significantly enhance the performance of a NO$_2$ gas sensor based on SnS$_2$ with nanoscale defects by photon illumination, and a detection limit of 2.5 ppb is achieved at room temperature. Using a classical Langmuir model and density functional theory simulations, we show S vacancies work as additional adsorption sites with fast adsorption times, higher adsorption energies, and an order of magnitude higher resistance change compared with pristine SnS$_2$. More interestingly, when electron–hole pairs are excited by photon illumination, the average adsorption time first increases and then decreases with NO$_2$ concentration, while the average desorption time always decreases with NO$_2$ concentration. Our results give a deep understanding of photo-enhanced gas sensing of SnS$_2$ with nanoscale defects, and thus open an interesting window for the design of high performance gas sensing devices based on 2D materials.

Nitrogen dioxide (NO$_2$) is one of the most common hazardous gas pollutants produced as a by-product of industry.[1–4] Notably, NO$_2$ is also a product yielded from the thermal decomposition of organic nitrates, such as TNT, which is a useful fingerprint for controlling these substances and combating international terrorism.[5] An issue of global concern, serious respiratory diseases can be caused by chronic environmental exposure to as little as 53 ppb NO$_2$.[1,4,6] Therefore, the research and development of gas sensors with high sensitivities is always of high priority.[2,7–19] Recently, 2D materials have been used for gas sensing owing to their large surface-to-volume ratios.[13,20] A wide variety of 2D materials, such as graphene,[9,10,14] black

phosphorus,[2,21] metal dichalcogenides,[4,12,15,18,19,22–24] have been studied as high performance gas sensors.[16,20,23,25,26]

As a member of the wide class 2D materials, tin disulfide (SnS$_2$) displays many intriguing properties in electronics,[27] photonics and optoelectronics,[27–30] as well as gas monitoring.[24,31–42] It was reported recently by Kalantar-zadeh *et al.* that a SnS$_2$-based NO$_2$ gas sensor with a sensitivity of 0.5 ppm could be improved to 30 ppb when heated to 120 °C.[24] However, an elevated operating temperature typically increases power consumption and thus a more intricate setup is required.[3,10,16,20,24,25,43] Furthermore, the high operating temperature might pose the risk of ignition when detecting in flammable or explosive atmospheres which would limit sensor's application.[44–46] Concurrently, it is known that 2D materials produced by chemical vapor deposition (CVD) usually contain nanoscale defects, such as vacancies, grain boundaries, *etc.* and in particular CVD grown SnS$_2$ is reported to naturally contain S vacancies.[47] It is well known that nanoscale defects can significantly affect gas sensing performance.[48] Thus it is important to investigate how S vacancies in SnS$_2$ affect the gas sensing performance. Furthermore, it should be also noted that compared with thermally assisted gas sensing, a photon assisted arrangement can not only improve the detection limit of gas sensor but also can accelerate the desorption ratio.[15,19,49–51] It is reported that SnS$_2$ nanosheets exhibit excellent optoelectronics properties,[27–30] making it feasible to improve the gas sensing performance of SnS$_2$ with photon illumination.

aSchool of Physics, Beijing Institute of Technology, Beijing 100081, P. R. China. E-mail: wuhc@bit.edu.cn

bDepartment of Physics, National Taiwan University, Taipei 106, Taiwan. E-mail: crchang@phys.ntu.edu.tw

cDepartment of Chemical Engineering & Materials Science, Yuan Ze University, Taoyuan City 320, Taiwan. E-mail: hrfuh@saturn.yzu.edu.tw

dInstitute of Plasma Physics, Chinese Academy of Sciences, Hefei 230031, P. R. China

eSchool of Chemical Engineering and Technology, Tianjin University, Tianjin 300072, P. R. China

fWestern Seoul Center, Korea Basic Science Institute, Seoul 03579, Republic of Korea

gChuncheon Center, Korea Basic Science Institute, Chuncheon 24341, Republic of Korea

hDivision of Industrial Metrology, Korea Research Institute of Standards and Science, Daejeon 305-340, Republic of Korea

† Electronic supplementary information (ESI) available. See DOI: 10.1039/c8ra08857h

In this work, we demonstrate that photon illumination can significantly enhance the performance of NO_2 gas sensors based on SnS_2, and an ultra-low concentration sensitivity of 2.5 ppb is achieved at room temperature. The results also show that gas sensitivity increases linearly with decreasing SnS_2 nanosheet thickness. In combination with a classical Langmuir model and density functional theory simulations, we show that S vacancies work as additional adsorption sites with fast adsorption times, higher adsorption energies, and greater resistance change compared with pristine SnS_2. Moreover, when electron–hole pairs are excited by photon illumination, the average adsorption time first increases and then decreases with NO_2 concentration. Considering safety, energy efficiency and sensitivity, SnS_2-based photo-illuminated gas sensors provide a possible way to realize the measurement of ultra-low concentrations of NO_2, or other hazardous gases, for environmental, industrial and domestic monitoring.

Fig. 1(a) shows a schematic of the chemical vapor deposition (CVD) arrangement for the SnS_2 nanosheet growth. A sulfur powder source was placed upstream in the furnace. Sn granules were smashed into pieces and were placed at the center of the furnace. Several pieces of a diced 300 nm SiO_2/Si (1 cm × 1 cm) wafer were placed downstream as substrates for SnS_2 growth. Further details of the SnS_2 growth can be found in the Experimental section. After the reaction, SnS_2 nanosheets were formed on the SiO_2/Si substrates. Fig. 1(b) shows a scanning electron microscopy (SEM) image of a SnS_2 flake grown on a SiO_2/Si substrate. The flakes typically have a semi-hexagonal structure with lateral dimensions ranging from 10 μm to 228 μm (Fig. S1†). Fig. 1(c) gives the structure of SnS_2 with the purple and yellow spheres representing Sn and S atoms, respectively.

Atomic force microscopy (AFM) was used to determine the thicknesses of the nanosheets. Fig. 2(a) shows the height profile of an ultrathin SnS_2 nanosheet with a thickness $\approx$ 6 nm ($\approx$10 layers, 0.6 nm per layer),[30] as measured along the red dotted line in the inset image, (more examples in Fig. S2†). The SnS_2 was also characterized by Raman spectroscopy, as shown in

Fig. 2(b). Only a single Raman peak (A_{1g} mode at 314 cm^{-1}) can be clearly observed for an 8 nm thick SnS_2 nanosheet, and an additional Raman peak, the E_g mode at 205 cm^{-1}, appears for a thicker 60 nm SnS_2 nanosheet, which is consistent with literature.[28,52] The E_g mode is due to the scattering centers for in-plane scattering. When the thickness drops below 8 nm the intensity decreases and effectively becomes undetectable.[30] The crystal structure of few-layer SnS_2 was further characterized by high-resolution transmission electronic microscopy (HRTEM), indicating the single-crystalline structure of the SnS_2 (Fig. 2(c)). The measured width of the lattice fringes is $\approx$ 0.32 nm which corresponds to the (100) plane of SnS_2. Fig. 2(d) shows the selected-area-electron-diffraction (SAED) pattern, which displays six-fold symmetry diffraction spots, confirming the hexagonal single-crystalline nature of the flake. Additionally, Sn and S elemental mapping using Electron Energy Loss Spectroscopy (EELS), in Fig. 2(f), of the selected area shown in Fig. 2(e), indicates the atomic ratio of Sn : S $\approx$ 1 : 1.86, suggesting the presence of S vacancies in the SnS_2, which is consistent with earlier reports.[47]

Before studying the photo-enhanced gas sensing properties of SnS_2, we first explored its optoelectronic properties. Fig. 3(a) is an optical image of a typical device prepared from a semi-hexagonal SnS_2 nanosheet on a SiO_2/Si substrate with 300 nm thick SiO_2. Fig. 3(b) shows the current *versus* voltage I_{DS}–V_{DS} (DS, Drain–Source) characteristics of the device with the gate voltage (V_G) varied from −20 V to 20 V in steps of 5 V and Fig. 3(c) plots the relationship between I_{DS} and V_G, with V_{DS} ranging from −10 V to +10 V in steps of 2.5 V indicating transfer characteristics of the device. From Fig. 3(b and c) it is apparent that our CVD grown SnS_2 nanosheets are n-type and the mobility is around 9.7 cm^2 V^{-1} s^{-1} which further supports the presence of the S vacancies.[47] Fig. 3(d and e) shows the I–V characteristics of the device at $V_G = 0$ V in the dark and under illumination by 532 nm and 650 nm lasers, in ambient conditions. It is found there is a notable change in the I_{DS} response going from dark to illuminated, and the enhancement of I_{DS} for the 532 nm laser is relatively larger than that observed for the 650 nm laser. Fig. 3(f) further shows the time resolved photo response of another device at $V_{DS} = 5$ V, where the light intensity of the 532 nm laser was 3.0 mW cm^{-2}. The responsivity (R_λ) and external quantum efficiency (EQE) are calculated to be 31 A W^{-1} and 7.7 × 10^3%, respectively (details of this calculation can be found in ESI Formula (2)†).

Fig. 4(a) is an optical image of a typical SnS_2-based gas sensor fabricated by conventional UV-lithography. The distance between each of the contacts is approximately 5 μm. Fig. 4(b and c) show the dynamic-sensing responses without and with 405 nm laser irradiation, respectively, where the NO_2 gas concentration was varied from 6.5 ppb to 130 ppb. The sensor response is defined as $\Delta R/R_0 = (R_{NO_2} - R_{N_2})/R_{N_2}$, where R_{N_2} and R_{NO_2} are the resistances of the device when exposed to pure N_2 and a NO_2 gas mix, respectively. In the dark environment, the sensor has the first observable response at 78 ppb NO_2. Remarkably, by illuminating the sensor with a 405 nm laser a clear response is observed at 13 ppb NO_2. To confirm this, Fig. 4(d) plotted I_{DS}–V_{DS} curves of the same device under
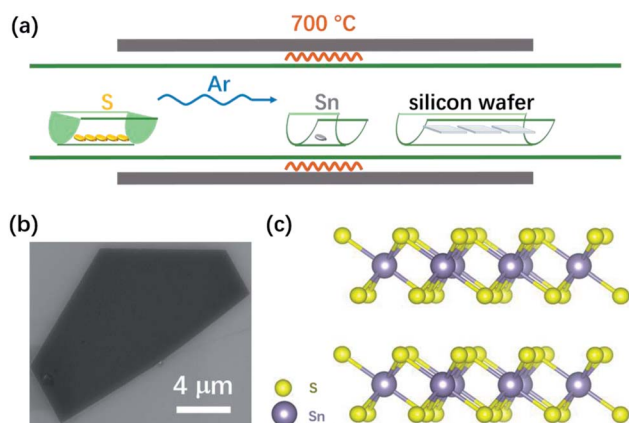

Fig. 1 (a) A schematic of CVD growth setup. (b) A SEM image of a semi-hexagonal nanosheet of SnS_2. (c) Schematic of SnS_2 structure with purple and yellow spheres representing Sn and S atoms, respectively.
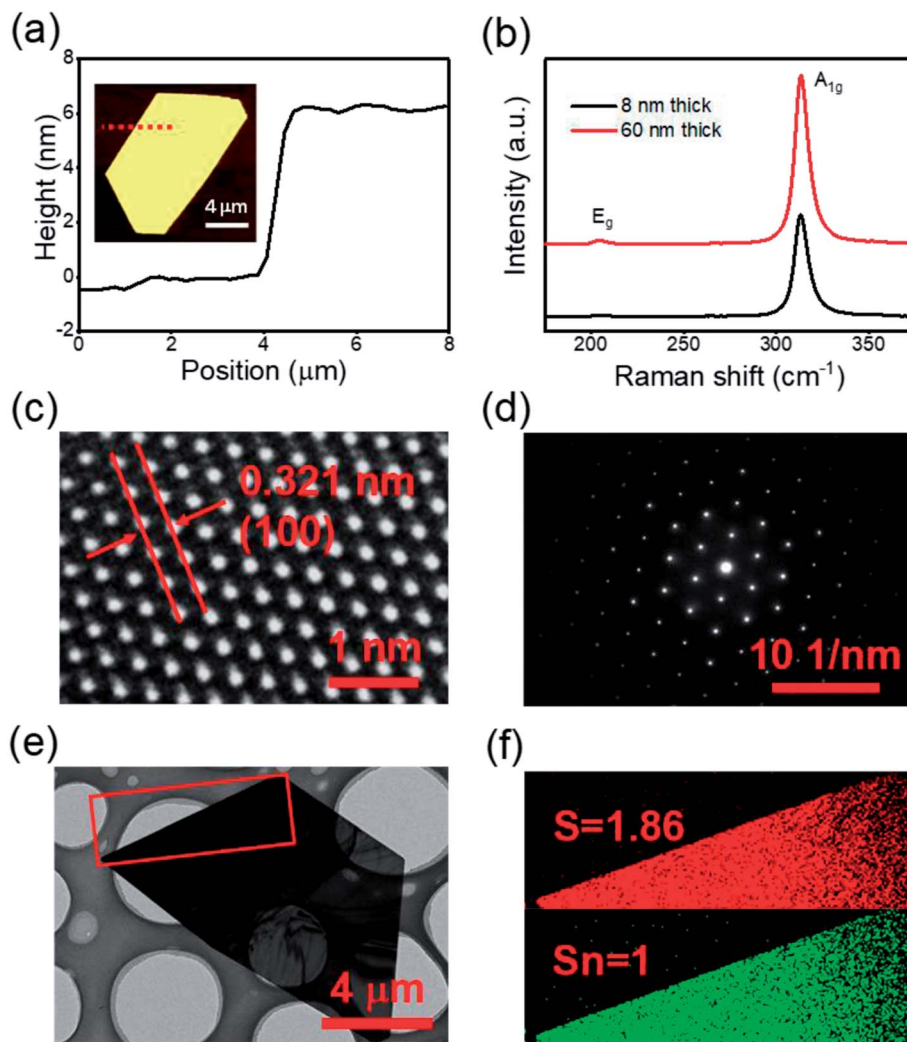
Fig. 2 Characterization of CVD produced single crystal SnS_2 nanosheet. (a) Height profiles of the dashed line shown in the inset AFM image. (b) Raman spectra of SnS_2 nanosheet. (c) High-resolution TEM image and corresponding (d) selected-area-electron-diffraction (SAED) pattern of a typical grown SnS_2 flake. (e) Low magnification bright field TEM image of a semi-hexagonal SnS_2 nanosheet. (f) EELS elemental mapping of the selected area in (e) with the result Sn : S = 1 : 1.86.

different NO_2 concentrations. It is apparent that in the dark environment, the I_{DS}–V_{DS} curves for 0 ppb, 26 ppb and 52 ppb NO_2 merge together. In contrast with this, clear distinctions can be observed between 0 ppb, 26 ppb and 52 ppb NO_2 with 405 nm laser illumination. A similar effect was observed with 650 nm (26 ppb) and 785 nm (52 ppb) lasers (Fig. S3†). Thus, laser illumination can improve the gas sensing capabilities of such devices.

The stability of a sensor is critical for practical applications. Multi-cycle dynamic sensing responses of the SnS_2-based sensor against to 13, 39 and 78 ppb NO_2 are used here to demonstrate the good repeatability and reproducibility of such SnS_2-based sensors (Fig. 4(e)). Moreover, the response to varied concentrations of NO_2 with a relative humidity 64% is also showed in Fig. S5(d).† These indicate the reliability of the illuminated SnS_2-based sensor and that the presence of water does not degrade performance.

To probe the function of sensitivity *versus* the thickness of SnS_2, we also tested more than 10 samples with different

thicknesses, ranging from 17 nm to 370 nm (Fig. S4–S9†). It is found that the sensitivity increases linearly as the thickness of the SnS_2-nanosheets is reduced, as shown in Fig. 4(f). Remarkably, a significant response is unmistakably observed at 2.5 ppb NO_2 for a 22 nm thick SnS_2 based gas sensor (Fig.-S8(d)†), suggesting that SnS_2 based gas sensor can achieve a NO_2 detection limit better than 2.5 ppb. To the best of our knowledge, this is the lowest detection limit for NO_2 achieved using SnS_2 devices to date, which is an improvement by a factor greater than ten on previous work.[24] Table 1 summarizes and compares the important features of SnS_2-based NO_2 gas sensors from literature. Kalantar-zadeh *et al.* heated their SnS_2 flake sensor to 120 °C to achieve a 30 ppb detection limit.[24] Hao *et al.* heated a SnS_2 flower interspersed with SnO_2 to 100 °C to reach a 125 ppb detection limit.[31] Ahn *et al.* built utilized vertical SnS_2 flake structures to detect NO_2 at 300 ppb, probably under its optimum conditions at 160 °C.[39] Li *et al.* heated SnS_2 their flake devices to 120 °C to attain a 600 ppb detection limit.[40] Wang *et al.* heated a SnS_2–SnO_2 composite flake device to 80 °C for

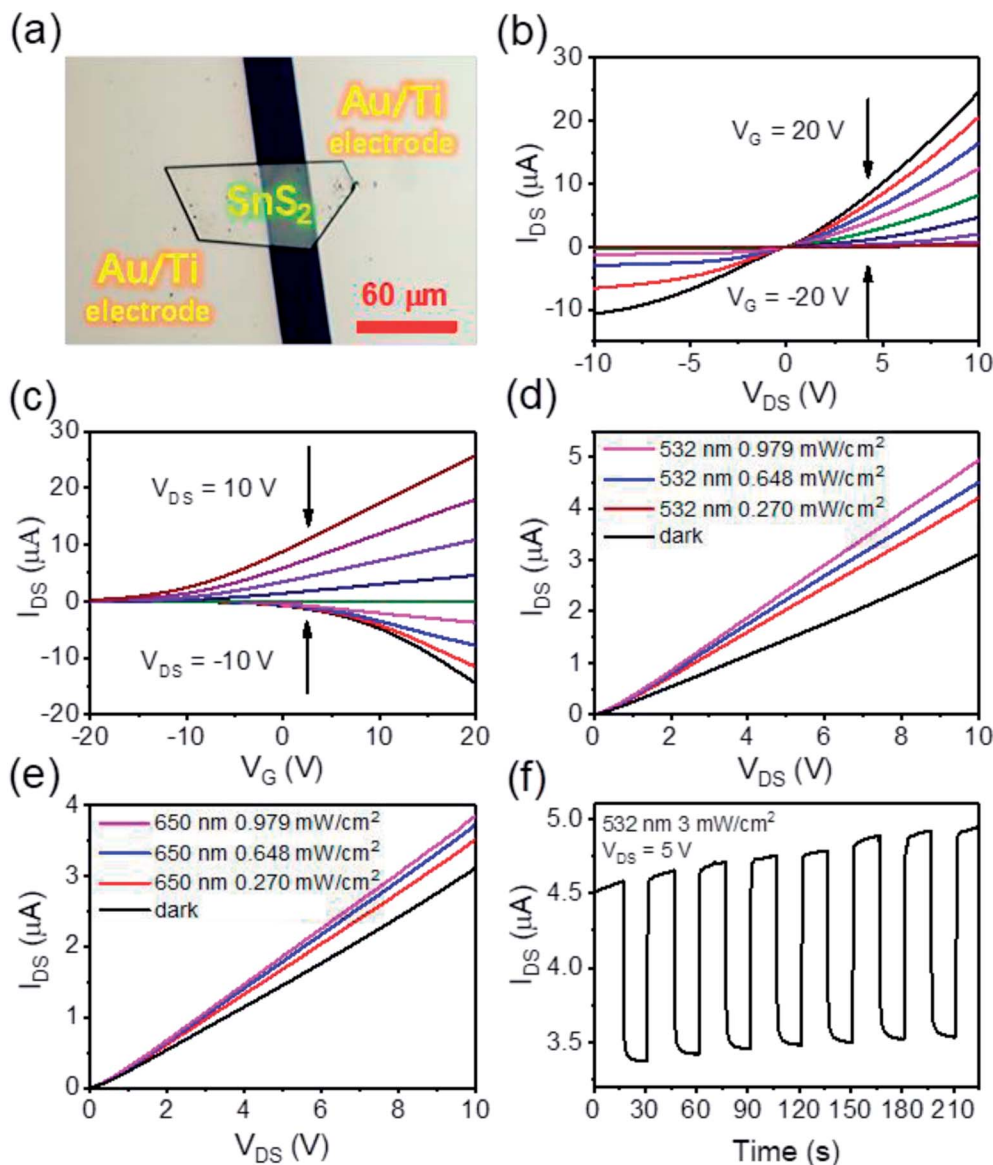**Fig. 3** (a) Optical microscope image of a SnS$_2$ device for the following measurement. (b) I_{DS}–V_{DS} curves for different V_G from −20 to 20 V in steps of 5 V. (c) I_{DS}–V_G curves for different V_{DS} from −10 to 10 V in steps of 2.5 V. (d) I_{DS}–V_{DS} curves of device under 532 nm laser illumination by different energy densities. (e) I_{DS}–V_{DS} curves of device under 650 nm laser illumination by different energy densities. (f) Time-resolved photon response of another SnS$_2$ device measured in vacuum (V_{DS} = 5 V, 532 nm laser 0.979 mW cm^{-2}).

a 1000 ppb detection limit.[41] While Xue *et al.* used SnS$_{1.5}$/Se$_{0.5}$ flake devices to detect 1000 ppb NO$_2$ at room temperature.[42]

To better illustrate the photo-enhanced gas sensing properties, we summarized the signal/noise (S/N) ratios of the $\Delta R/R_0$ from response in Fig. 4(b and c) into Fig. 5(a).[53–57] It is clear that there are 3 distinct regions. At high concentrations of NO$_2$ the S/N is almost constant (dark and 785 nm). This means the surface adsorption is almost saturated and has reached its upper limit. Increasing gas concentration does not increase the signal. In the medium concentration range (classic region), S/N increases linearly with gas concentration. In the low NO$_2$ concentration regime (<52 ppb) no effective signal is detected for dark conditions. But a signal is detected with illumination, which is especially prominent for the short wavelength light, indicating extra energy is required to desorb NO$_2$ from surface of SnS$_2$.

We fitted the desorption (adsorption) sections of the dynamic-sensing response curves under different laser illuminations with the expression $y = y_0 + A\mathrm{e}^{\frac{-x}{\tau_D}}$ $\left(y = y_0 + A\mathrm{e}^{\frac{x}{\tau_A}} \right)$, where τ_D (τ_A) is the average desorption (adsorption) time. The average desorption times and average adsorption times under various laser illuminations are summarized in Fig. 5(b) and (c) respectively. It is clear illumination not only enables ultra-high sensitivity but also results in faster desorption and better S/N ratios. Interestingly, with the 405 nm laser illumination, the adsorption time first increases and then decreases with gas concentration when the concentration reaches ∼78 ppb. While for dark and 785 nm laser illumination, both the desorption and adsorption times decrease with increasing gas concentration.
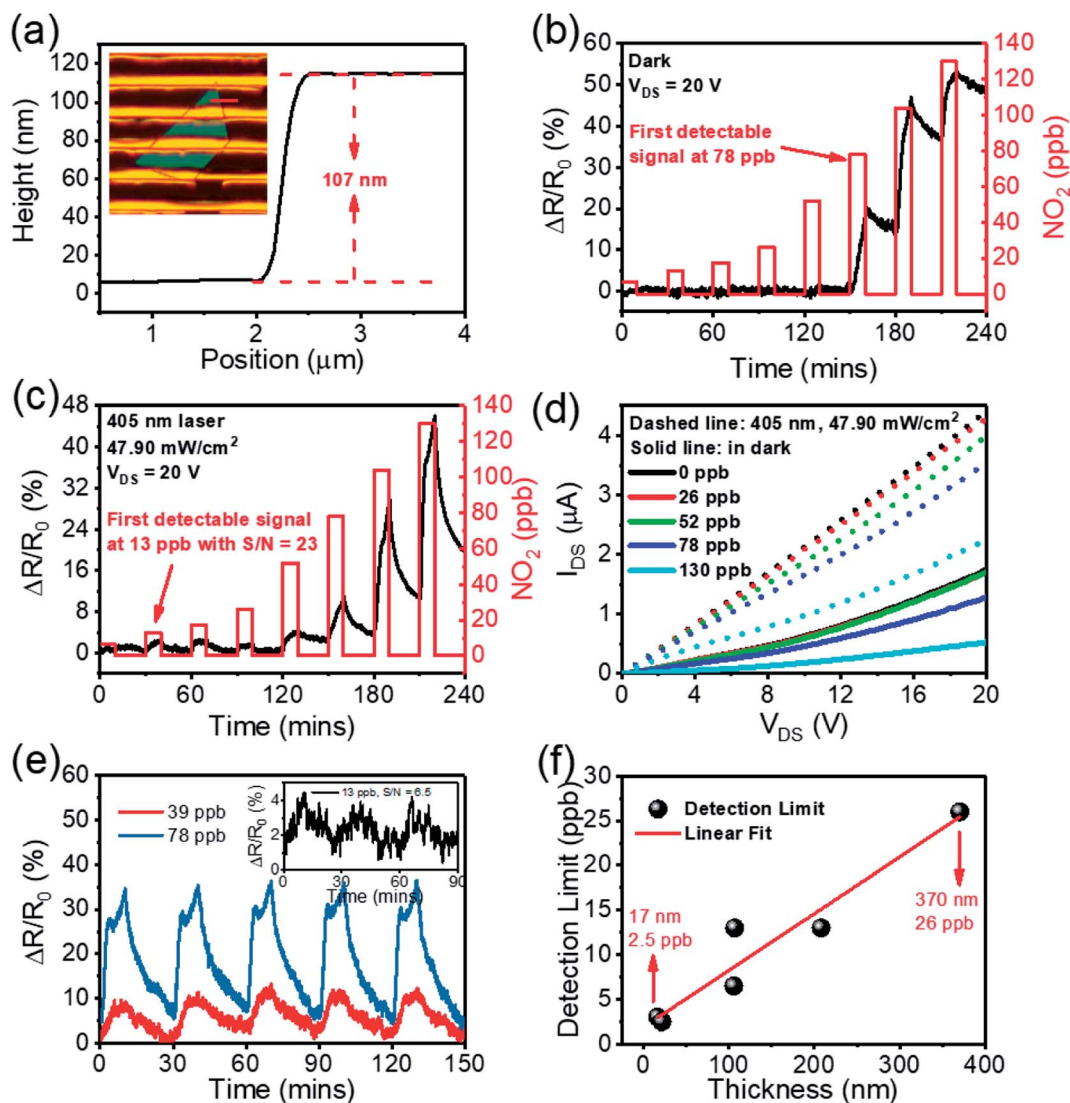
Fig. 4   (a) Optical microscope image of a SnS$_2$ device for gas sensor measurements. Dynamic sensing response of $\Delta R/R_0$ change *versus* time for the SnS$_2$-based sensor upon exposure to NO$_2$ gas with concentrations ranging from 6.5 ppb to 130 ppb under (b) dark environment and (c) 405 nm laser irradiation. (d) Comparison $I_{DS}-V_{DS}$ curves of the device under different light illuminations and NO$_2$ concentrations. (e) Multi-cycle responses of sensor when exposed to concentrations of 13, 39, and 78 ppb NO$_2$. (f) Sensitivity as a function of SnS$_2$ thickness.

We replotted the dynamic-sensing response curves under 405 nm laser illumination based on the Langmuir model (Fig. 6).[58] There are two classes of adsorption sites. Similar behavior has been observed under 785 nm and 650 nm laser illumination (Fig. S10†). For the adsorption process, NO$_2$ can adsorb on both sites but prefer sites with fast adsorption times. With increasing gas concentration, more NO$_2$ molecules will be adsorbed on sites with slower adsorption times which increases the average adsorption time. At yet higher gas concentrations all the fast adsorption time sites will be occupied. The NO$_2$

Table 1   Comparison of NO$_2$ gas sensors performance for SnS$_2$-based sensors. Our SnS$_2$ gas sensor achieves a remarkably detection limit more than 10 times better than values reported in previous works

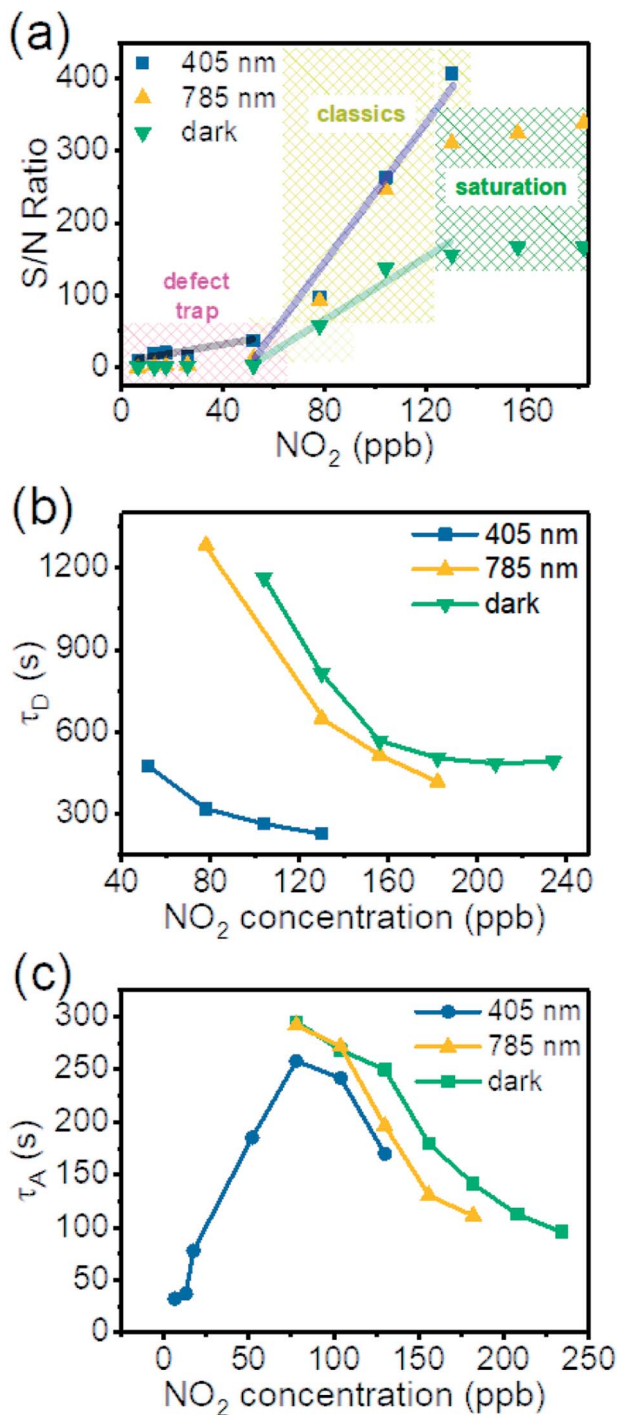| No.	Material	Limit of detection	Special method	Reference
1	SnS$_2$ flake	2.5 ppb	UV illumination	This work
2	SnS$_2$ flake	30 ppb	Heater	24
3	SnS$_2$/SnO$_2$ flakes	125 ppb	Heater	31
4	SnS$_2$ flakes	300 ppb	Heater	39
5	SnS$_2$ flakes	600 ppb	Heater	40
6	SnS$_2$/SnO$_2$	1000 ppb	Heater	41
7	SnS$_{1.5}$/Se$_{0.5}$	1000 ppb	Room temperature	42

Fig. 5 (a) Comparison of S/N ratio of the dynamic response of the SnS$_2$ sensor for dark and illuminated environments. Green line is a linear fitting of dark environment data between 52 to 130 ppb NO$_2$. Black line and blue line are linear fitting of 405 nm illumination data between 6.5 to 52 ppb and 52 to 130 ppb NO$_2$. (b) Desorption time as a function of gas concentration. (c) Adsorption time as a function of gas concentration.

molecules will be adsorbed on the sites with slow adsorption times, which can be treated as one site adsorption. According to the Langmuir model considering one adsorption site, $\tau_D = \dfrac{1}{aN_c}$, where N_c is proportional to the gas concentration.

This is why the average adsorption time first increases and then decreases with gas concentration. On the other hand, for the desorption process at low concentrations it is the sites with slow desorption times that are the limiting factor. With increasing gas concentration, more molecules will be desorbed from the sites with faster desorption times, thus decreasing the average desorption time. Moreover, NO$_2$ molecules absorb on sites with faster adsorption times will significantly decrease the overall conductance compared with NO$_2$ molecules bound to sites with slow adsorption.

To investigate whether S vacancies could give such an effect, we calculated the adsorption energy, charge density distribution, and conductance of NO$_2$ molecules on a SnS$_2$ monolayer with and without S vacancies. Details of the calculations can be found in the Methods section. Fig. 7(a) and (b) show the optimized atomic structures of a NO$_2$ molecule adsorbed on pristine SnS$_2$ and SnS$_2$ with a surface S vacancy respectively. For a NO$_2$ molecule adsorbed on pristine SnS$_2$, the perpendicular distance between the O atom of a NO$_2$ molecule and the nearest S atom of the SnS$_2$ (R) is about 2.95 Å and it is decreased significantly to 0.5 Å for a NO$_2$ molecule on SnS$_2$ with a S vacancy, indicating the S vacancy induces strong adsorption between SnS$_2$ and NO$_2$. To understand the adsorption mechanism, the adsorption energy as a function of distance R is plotted in Fig. 7(c). The adsorption energy is 1.011 eV when a NO$_2$ molecule adsorbed on SnS$_2$ with a S vacancy. While for a NO$_2$ molecule adsorbed on pristine SnS$_2$, the corresponding adsorption energy is only 116 meV. Thus, NO$_2$ molecules adsorbed on the SnS$_2$ monolayer with S vacancies have a larger adsorption energy compared with a pristine SnS$_2$ monolayer, indicating that extra energy is required to desorb NO$_2$ molecule from the S vacancy site (Fig. 7(d)). The adsorption energy for chemisorption is usually an energy of 1–10 eV, but for physisorption the energy is smaller than this. Therefore, the adsorption mechanism may change from physisorption to chemisorption when a NO$_2$ molecule adsorbed on SnS$_2$ with S vacancy. Moreover, there is a large partial charge transfer between S and the O atoms of a NO$_2$ molecule adsorbed on SnS$_2$ with S vacancy in Fig. 7(e) and (f).

The electrical conductivity of an NO$_2$ molecule adsorbed on pristine SnS$_2$ and on SnS$_2$ with a single S vacancy at 300 K are shown in Fig. 8. We found that monolayer SnS$_2$ contains a narrow electrical conductivity tail near $\mu = 0$ resulting from electrons crossing the Fermi level from thermal agitation at $T = 300$ K, shown in Fig. 8(a). When this pristine SnS$_2$ adsorbs an NO$_2$ molecule there is an additional conductivity peak region near $\mu = 0$ with small values of 1.1×10^3 and 3.0×10^2 $(1/\Omega\ \mathrm{m^{-1}})$ for σ_{xx} and σ_{yy}, respectively, as shown in Fig. 8(b). However for SnS$_2$ with a S vacancy adsorbing a NO$_2$ molecule, there is a broad additional conductivity region around $\mu = 0$ with values about 1.5×10^4 and 1.9×10^4 $(1/\Omega\ \mathrm{m^{-1}})$ for σ_{xx} and σ_{yy}, respectively, shown in Fig. 8(c). These results from transport and DFT analysis are consistent with the experimental conclusions on the resistance changes, and also indicate charge transfer between NO$_2$ and SnS$_2$ is critical. It also suggests that the sites with fast adsorption times are S vacancies and the sites with slow adsorption times are the areas of pristine SnS$_2$. To
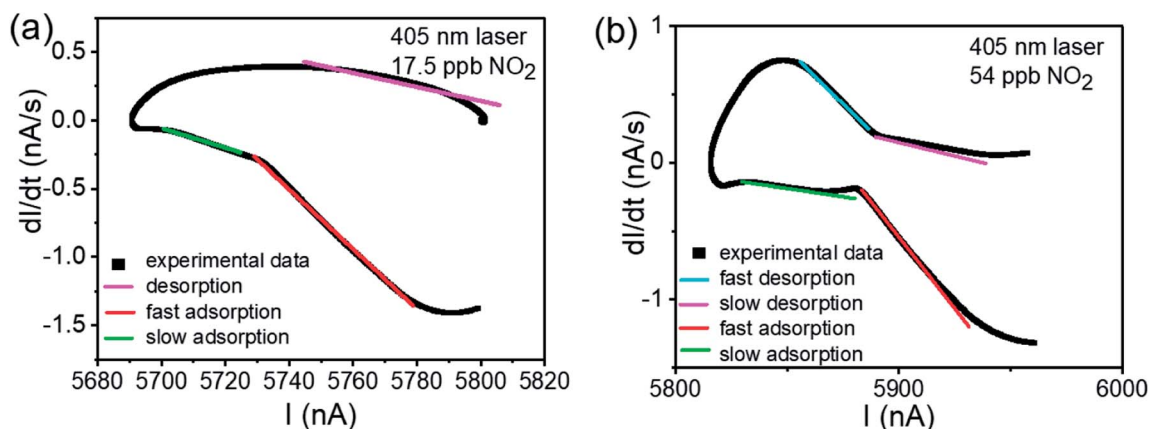
Fig. 6 The dI/dt–I relationship of Fig. 4(c). (a) The dI/dt–I curve of 17.5 ppb NO_2 test. (b) The dI/dt–I curve of 54 ppb NO_2 test. In both of two picture, the fitting lines are shown, with blue line depicting the fast desorption process, violet line depicting slow desorption process, red line depicting fast adsorption process and green line depicting slow adsorption process.
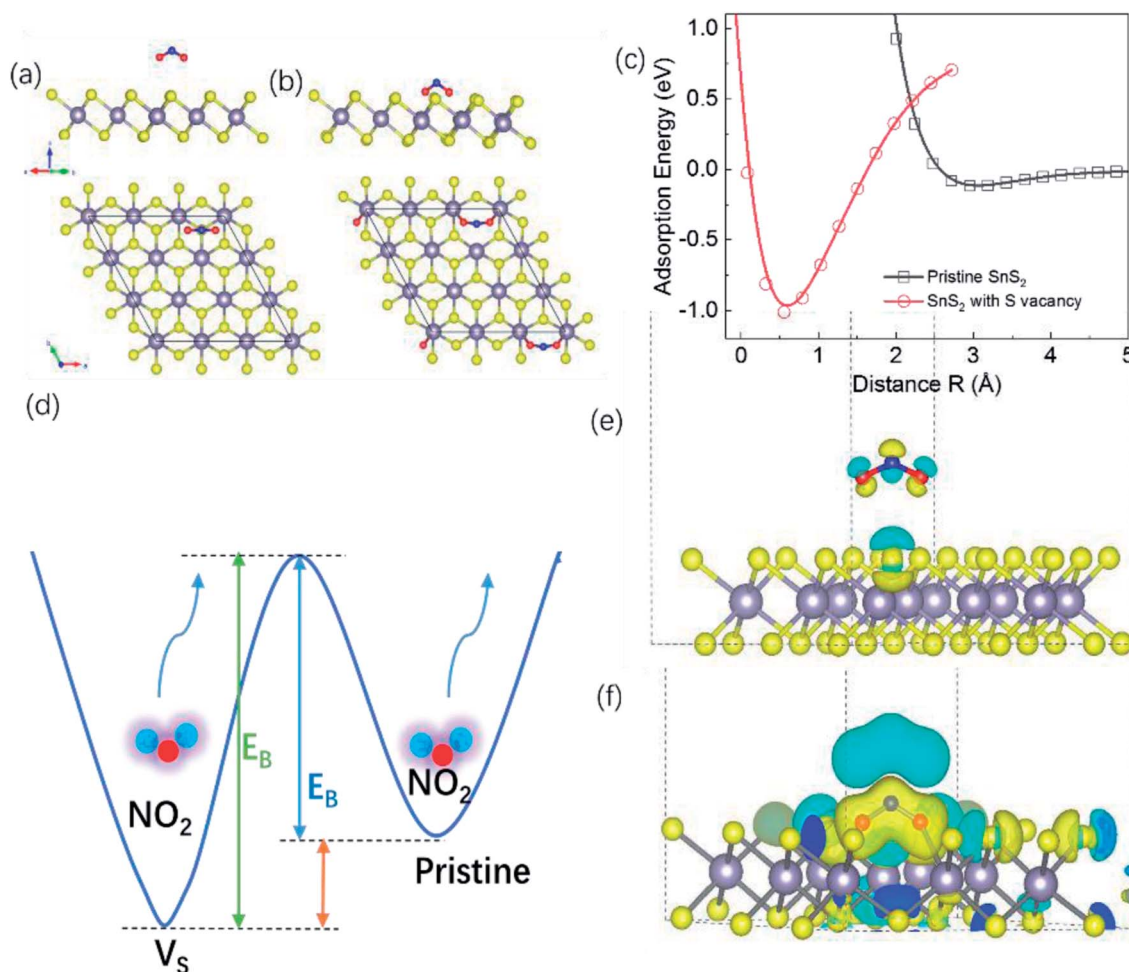

Fig. 7 (a) and (b) Side view and top view of the atomic structure of NO_2 molecule adsorbed on Sn_9S_{18} and Sn_9S_{17} surfaces, respectively. The large dark spheres represents Sn atoms, while the yellow, blue and red spheres represent the S, N and O atoms, respectively. (c) Adsorption energy as a function of distance R (defined as the perpendicular distance between the O atom of NO_2 molecule and the nearest S atom of the SnS_2) for NO_2 molecule adsorbed on Sn_9S_{18} and Sn_9S_{17} surfaces. (d) Schematic of adsorption energies for an NO_2 molecule adsorbed on pristine SnS_2 and on SnS_2 with a S vacancy. (e) and (f) Charge density difference distribution for NO_2 molecule adsorbed on Sn_9S_{18} and Sn_9S_{17} surfaces, respectively. The charge density difference in yellow indicate increases in charge density, while blue indicates a decreases in charge density (isosurface = 0.0015 eV A^{-3}).

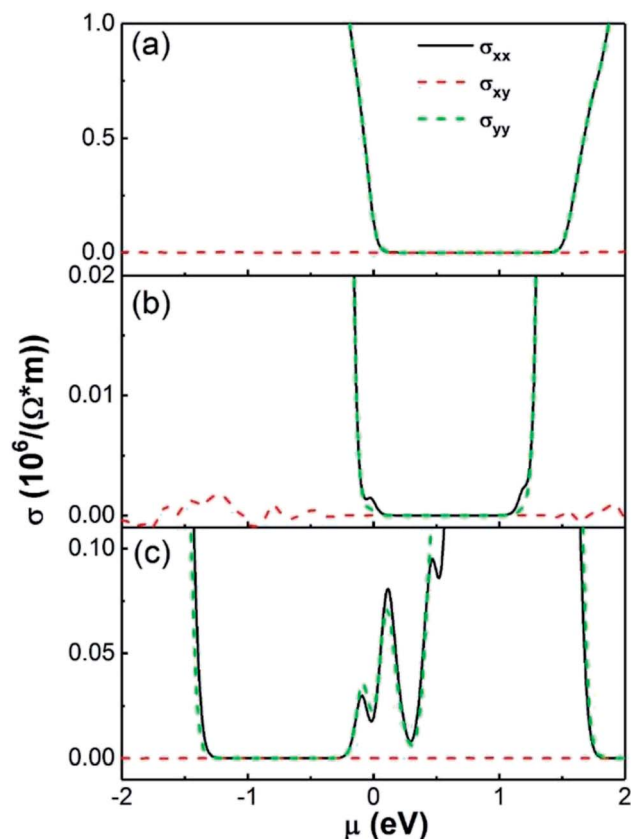Fig. 8 Electron conductivity of (a) SnS$_2$ monolayer (b) SnS$_2$ with adsorbed NO$_2$ molecule and (c) SnS$_2$ with S vacancy adsorbed NO$_2$ molecule which S vacancy concentration is 3.70% at 300 K.

further highlight the importance of S vacancies for the gas sensor performance, we measured the gas performance of gas sensors based on same thick SnS$_2$ but with different S vacancy density, where the density of S vacancies density was determined by mapping the whole sensor using the EDS equipped in the SEM chamber. A relatively low detection limit or high gas performance was achieved for the sample with higher S vacancies density. For example, for gas sensors based one 106 nm thick SnS$_2$, the detection limit for sensor with an atomic ratio of Sn : S $\approx$ 1 : 1.72 is 6.5 ppb and that for sensor with an atomic ratio of Sn : S $\approx$ 1 : 1.84 is 13 ppb. We would like to stress that the nanoscale defects are naturally occurring defects forming during chemical vapor deposition. Therefore, they are quite stable when interacting with NO$_2$ molecules.

It is reported that Schottky junction[59,60] and photo-excited electron–hole pairs can contribute the gas sensing performance. Since our gas sensing performance depends crucially on the wavelength of the photons and same bias voltage is used, here we focus our discussion on effect due to photo-excited electron–hole pairs. We measured the gas sensing performance of another sensor under 365, 405, and 650 nm laser illuminations (Fig. S11†). Only 365 and 405 nm lasers can excite electron–hole pairs, because the band gap of SnS$_2$ is around 2.2 eV. The 365 and 405 nm laser illuminations have similar detection limit, better than 650 nm. More importantly, the average adsorption time first increases and then decreases with

NO$_2$ concentration under the 365 and 405 nm laser illuminations, indicating the importance of photo-excited electron–hole pairs for the charge transfer process upon NO$_2$ adsorption. Therefore, the observed distinct behavior of the adsorption time may be due to the photo-excited electron–hole pairs. We would like to stress that the average adsorption time is faster under the 405 nm photo illumination than the 365 nm, indicating that the 405 nm laser illumination is more efficient since the adsorption spectrum of NO$_2$ peaks at $\sim$400 nm at 293 K.[61]

In summary, NO$_2$ gas sensors were fabricated based on CVD grown SnS$_2$. An ultra-high sensitivity of 2.5 ppb at room temperature was achieved by utilizing inherent defects under photon illumination. Our results further show S vacancies in SnS$_2$ work as additional adsorption sites and the detection limit, signal to noise (S/N) value, and desorption time can be significantly improved by photo illumination, thus providing a plausible way to design high performance gas sensors based on 2D materials with nanoscale defects.

Method

The detailed experiments and characterizations are shown in the ESI.†

Author contributions

H. C. W. conceived the study. D. Y. C., and Y. L. L. grew the sample. W. J. Y., H. J. X. and Z. W. fabricated the sample. J. C., M. C., and B. S. C. carried out the TEM measurements. W. J. Y. and C. C. performed the gas sensing measurements. H. R. F. and C. R. C. conducted the DFT simulation. Z. T. J. and H. J. L. gave scientific advice. H. C. W., W. J. Y., D. Y. C., and C. C. wrote the manuscript. All authors discussed the results and commented on the manuscript.

Conflicts of interest

There no conflicts to declare.

Acknowledgements

References

1 B. Liu, L. Chen, G. Liu, A. N. Abbas, M. Fathi and C. Zhou, *ACS Nano*, 2014, **8**(5), 5304–5314.

2 A. N. Abbas, B. Liu, L. Chen, Y. Ma, S. Cong, N. Aroonyadet, M. Köpf, T. Nilges and C. Zhou, *ACS Nano*, 2015, **9**(5), 5618–5624.

3 S. S. Shendage, V. L. Patil, S. A. Vanalakar, S. P. Patil, N. S. Harale, J. L. Bhosale, J. H. Kim and P. S. Patil, *Sens. Actuators, B*, 2017, **240**, 426–433.

4 T. Xu, Y. Pei, Y. Liu, D. Wu, Z. Shi, J. Xu, Y. Tian and X. Li, *J. Alloys Compd.*, 2017, **725**, 253–259.

5 C. Hao, P. B. Shepson, J. W. Drummond and K. Muthuramu, *Anal. Chem.*, 1994, **66**(21), 3737–3743.

6 https://www.epa.gov/criteria-air-pollutants/naaqs-table.

7 J. Kong, N. R. Franklin, C. Zhou, M. G. Chapline, S. Peng, K. Cho and H. Dai, *Science*, 2000, **287**(5453), 622–625.

8 E. Rossinyol, A. Prim, E. Pellicer, J. Arbiol, F. Hernández-Ramírez, F. Peiró, A. Cornet, J. R. Morante, L. A. Solovyov, B. Tian, T. Bo and D. Zhao, *Adv. Funct. Mater.*, 2007, **17**(11), 1801–1806.

9 F. Schedin, A. K. Geim, S. V. Morozov, E. W. Hill, P. Blake, M. I. Katsnelson and K. S. Novoselov, *Nat. Mater.*, 2007, **6**(9), 652–655.

10 J. D. Fowler, M. J. Allen, V. C. Tung, Y. Yang, R. B. Kaner and B. H. Weiller, *ACS Nano*, 2009, **3**(2), 301–306.

11 S. Deng, V. Tjoa, H. M. Fan, H. R. Tan, D. C. Sayle, M. Olivo, S. Mhaisalkar, J. Wei and C. H. Sow, *J. Am. Chem. Soc.*, 2012, **134**(10), 4905–4917.

12 F. K. Butt, C. Cao, W. S. Khan, Z. Ali, R. Ahmed, F. Idrees, I. Aslam, M. Tanveer, J. Li and S. Zaman, *Mater. Chem. Phys.*, 2012, **137**(137), 565.

13 F. K. Perkins, A. L. Friedman, E. Cobas, P. M. Campbell, G. G. Jernigan and B. T. Jonker, *Nano Lett.*, 2013, **13**(2), 668–673.

14 W. Yuan, A. Liu, L. Huang, C. Li and G. Shi, *Adv. Mater.*, 2013, **25**(5), 766–771.

15 N. Huo, S. Yang, Z. Wei, S.-S. Li, J.-B. Xia and J. Li, *Sci. Rep.*, 2014, **4**, 5209.

16 H. Long, A. Harley-Trochimczyk, T. Pham, Z. Tang, T. Shi, A. Zettl, C. Carraro, M. A. Worsley and R. Maboudian, *Adv. Funct. Mater.*, 2016, **26**(28), 5158–5165.

17 J. Zhang, X. Liu, G. Neri and N. Pinna, *Adv. Mater.*, 2016, **28**(5), 795–831.

18 J. Baek, D. Yin, N. Liu, I. Omkaram, C. Jung, H. Im, S. Hong, S. M. Kim, Y. K. Hong, J. Hur, Y. Yoon and S. Kim, *Nano Res.*, 2017, **10**(8), 2904.

19 Z. Feng, Y. Xie, E. Wu, Y. Yu, S. Zheng, R. Zhang, X. Chen, C. Sun, H. Zhang, W. Pang, J. Liu and D. Zhang, *Micromachines*, 2017, **8**(5), 155.

20 B. Cho, J. Yoon, S. K. Lim, A. R. Kim, D.-H. Kim, S.-G. Park, J.-D. Kwon, Y.-J. Lee, K.-H. Lee, B. H. Lee, H. C. Ko and M. G. Hahm, *ACS Appl. Mater. Interfaces*, 2015, **7**(30), 16775–16780.

21 L. Kou, T. Frauenheim and C. Chen, *J. Phys. Chem. Lett.*, 2014, **5**(15), 2675–2681.

22 S. Weidong, H. Lihua, W. Haishui, Z. Hongjie, Y. Jianhui and W. Pinghui, *Nanotechnology*, 2006, **17**(12), 2918.

23 D. J. Late, T. Doneux and M. Bougouma, *Appl. Phys. Lett.*, 2014, **105**(23), 233103.

24 J. Z. Ou, W. Ge, B. Carey, T. Daeneke, A. Rotbart, W. Shan, Y. Wang, Z. Fu, A. F. Chrimes, W. Wlodarski, S. P. Russo, Y. X. Li and K. Kalantar-zadeh, *ACS Nano*, 2015, **9**(10), 10313–10323.

25 Y. Li, S. G. Leonardi, A. Bonavita, G. Neri and W. Wlodarski, *Procedia Eng.*, 2016, **168**, 1102–1105.

26 W. Yang, L. Gan, H. Li and T. Zhai, *Inorg. Chem. Front.*, 2016, **3**(4), 433–451.

27 Y. Huang, E. Sutter, J. T. Sadowski, M. Cotlet, O. L. A. Monti, D. A. Racke, M. R. Neupane, D. Wickramaratne, R. K. Lake, B. A. Parkinson and P. Sutter, *ACS Nano*, 2014, **8**(10), 10743–10755.

28 G. Su, V. G. Hadjiev, P. E. Loya, J. Zhang, S. Lei, S. Maharjan, P. Dong, P. M. Ajayan, J. Lou and H. Peng, *Nano Lett.*, 2015, **15**(1), 506–513.

29 J. Xia, D. Zhu, L. Wang, B. Huang, X. Huang and X.-M. Meng, *Adv. Funct. Mater.*, 2015, **25**(27), 4255–4261.

30 X. Zhou, Q. Zhang, L. Gan, H. Li and T. Zhai, *Adv. Funct. Mater.*, 2016, **26**(24), 4405–4413.

31 J. Hao, D. Zhang, Q. Sun, S. Zheng, J. Sun and Y. Wang, *Nanoscale*, 2018, **10**(15), 7210–7217.

32 D. Gu, X. Li, Y. Zhao and J. Wang, *Sens. Actuators, B*, 2017, **244**, 67–76.

33 R. Li, K. Jiang, S. Chen, Z. Lou, T. Huang, D. Chen and G. Shen, *RSC Adv.*, 2017, **7**(83), 52503–52509.

34 K. Xu, N. Li, D. Zeng, S. Tian, S. Zhang, D. Hu and C. Xie, *ACS Appl. Mater. Interfaces*, 2015, **7**(21), 11359.

35 H. Chen, Y. Chen, H. Zhang, D. W. Zhang, P. Zhou and J. Huang, *Adv. Funct. Mater.*, 2018, **28**(20), 1801035.

36 M. Ma, H. Khan, W. Shan, Y. Wang, J. Z. Ou, Z. Liu, K. Kalantar-zadeh and Y. Li, *Sens. Actuators, B*, 2017, **239**, 711–717.

37 Y. Xiong, W. Xu, D. Ding, W. Lu, L. Zhu, Z. Zhu, Y. Wang and Q. Xue, *J. Hazard. Mater.*, 2018, **341**, 159–167.

38 Z. Qin, K. Xu, H. Yue, H. Wang, J. Zhang, C. Ouyang, C. Xie and D. Zeng, *Sens. Actuators, B*, 2018, **262**, 771–779.

39 C. Kim, J. C. Park, S. Y. Choi, Y. Kim, S. Y. Seo, T. E. Park, S. H. Kwon, B. Cho and J. H. Ahn, *Small*, 2018, 1704116.

40 M. Ma, H. Khan, W. Shan, Y. Wang, J. Z. Ou, Z. Liu, K. Kalantar-zadeh and Y. Li, *Sens. Actuators, B*, 2017, **239**, 711–717.

41 D. Gu, X. Li, Y. Zhao and J. Wang, *Sens. Actuators, B*, 2017, **244**, 67–76.

42 Z. Yang, H. Liang, X. Wang, X. Ma, T. Zhang, Y. Yang, L. Xie, D. Chen, Y. Long and J. Chen, *ACS Nano*, 2015, **10**(1), 755–762.

43 B. Cho, M. G. Hahm, M. Choi, J. Yoon, A. R. Kim, Y.-J. Lee, S.-G. Park, J.-D. Kwon, C. S. Kim, M. Song, Y. Jeong, K.-S. Nam, S. Lee, T. J. Yoo, C. G. Kang, B. H. Lee, H. C. Ko, P. M. Ajayan and D.-H. Kim, *Sci. Rep.*, 2015, **5**, 8052.

44 D. Barreca, D. Bekermann, E. Comini, A. Devi, R. A. Fischer, A. Gasparotto, C. Maccato, G. Sberveglieri and E. Tondello, *Sens. Actuators, B*, 2010, **149**(1), 1–7.

45 J. Deng, Z. Luo, X. Wu and Y. Hu, *Min. Sci. Technol.*, 2010, **20**(4), 557–562.

46 Z. S. Hosseini, A. I. zad and A. Mortezaali, *Sens. Actuators, B*, 2015, **207**, 865–871.

47 Y. Gong, H. Yuan, C.-L. Wu, P. Tang, S.-Z. Yang, A. Yang, G. Li, B. Liu, J. van de Groep, M. L. Brongersma, M. F. Chisholm, S.-C. Zhang, W. Zhou and Y. Cui, *Nat. Nanotechnol.*, 2018, **13**(4), 294–299.

48 J. Shen, G. Liu, K. Huang, Z. Chu, W. Jin and N. Xu, *ACS Nano*, 2016, **10**(3), 3398–3409.

49 G. Chen, T. M. Paronyan, E. M. Pigos and A. R. Harutyunyan, *Sci. Rep.*, 2012, **2**, 343.

50 S. Park, S. An, H. Ko, S. Lee and C. Lee, *Sens. Actuators, B*, 2013, **188**, 1270–1276.

51 S. Park, S. An, Y. Mun and C. Lee, *ACS Appl. Mater. Interfaces*, 2013, **5**(10), 4285–4292.

52 J. H. Ahn, M. J. Lee, H. Heo, H. S. Ji, K. Kim, H. Hwang and M. H. Jo, *Nano Lett.*, 2015, **15**(6), 3703.

53 L. A. Currie, Quellenangabe, *Pure Appl. Chem.*, 1995, 1699–1723.

54 J. Li, Y. Lu, Q. Ye, M. Cinke, J. Han and M. Meyyappan, *Nano Lett.*, 2003, **3**(7), 929–933.

55 K. Lee, R. Gatensby, N. McEvoy, T. Hallam and G. S. Duesberg, *Adv. Mater.*, 2013, **25**(46), 6699–6702.

56 Y. Wu, D. Zhang, K. Lee, G. S. Duesberg, A. Syrlybekov, X. Liu, M. Abid, M. Abid, Y. Liu and L. Zhang, *Adv. Mater. Technol.*, 2016, 1600197.

57 P. E. Blöchl, *Phys. Rev. B: Condens. Matter Mater. Phys.*, 1994, **50**(24), 17953–17979.

58 C. Wen, Q. Ye, S.-L. Zhang and D. Wu, *Sens. Actuators, B*, 2016, **223**, 791–798.

59 M. Zhu, X. Li, S. Chung, L. Zhao, X. Li, X. Zang, K. Wang, J. Wei, M. Zhong, K. Zhou, D. Xie and H. Zhu, *Carbon*, 2015, **84**, 138–145.

60 H.-Y. Kim, K. Lee, N. McEvoy, C. Yim and G. S. Duesberg, *Nano Lett.*, 2013, **13**(5), 2182–2188.

61 J. P. Burrows, A. Dehn, B. Deters, S. Himmelmann, A. Richter, S. Voigt and J. Orphal, *J. Quant. Spectrosc. Radiat. Transfer*, 1998, **60**(6), 1025–1031.